Progress in Photovoltaics: Research and Applications

WILEY

PROGRESS IN PHOTOVOLTAICS

RESEARCH ARTICLE

CuIn $(Se,Te)_2$ Absorbers With Bandgaps <1 eV for Bottom Cells in Tandem Applications

Thomas Paul Weiss | Mohit Sood | Aline Vanderhaegen | Susanne Siebentritt

Laboratory for Photovoltaics, Department of Physics and Materials Science, University of Luxembourg, Belvaux, Luxembourg

Correspondence: Susanne Siebentritt (susanne.siebentritt@uni.lu)

Received: 13 May 2024 | **Revised:** 9 August 2024 | **Accepted:** 3 September 2024

Funding: Fonds National de la Recherche, Luxembourg within the project PRIDE15/10935404/MASSENA.

Keywords: chalcopyrite | low gap | tandem solar cells

ABSTRACT

Thin-film solar cells reach high efficiencies and have a low carbon footprint in production. Tandem solar cells have the potential to significantly increase the efficiency of this technology, where the bottom-cell is generally composed of a $Cu(In,Ga)Se_2$ absorber layer with bandgaps around 1 eV or higher. Here, we investigate $CuIn(Se_{1-x}Te_x)_2$ absorber layers and solar cells with bandgaps below 1 eV, which will bring the benefit of an additional degree of freedom for designing current-matched two-terminal tandem devices. We report that $CuIn(Se_{1-x}Te_x)_2$ thin films can be grown single phase by co-evaporation and that the bandgap can be reduced to the optimum range (0.92–0.95 eV) for a bottom cell. From photoluminescence spectroscopy, it is found that no additional non-radiative losses are introduced to the absorber when adding Te. However, V_{OC} losses occur in the final solar cell due to non-optimized interfaces. Nevertheless, a device with 9% power conversion efficiency is demonstrated with a bandgap of 0.97 eV and $x = 0.07$, the highest efficiency so far for chalcopyrites with band gap <1 eV. Interface recombination is identified as a major recombination channel for larger Te contents. Thus, further efficiency improvements can be expected with improved absorber/buffer interfaces.

1 | Introduction

Compound thin film photovoltaics (PV) enable high power conversion efficiency in combination with a low carbon footprint [1] and are therefore an important technology to mitigate the climate crisis. Ideal single-junction solar cells are limited to power conversion efficiencies below 33% as demonstrated by the Shockley–Queisser limit [2], whereas multi-junction solar cells allow to reach higher efficiencies. The reasons are lower thermalization losses and the possibility to use a larger range of the solar photon spectrum. The highest photovoltaic efficiencies are indeed achieved by multi-junction solar cells [3]. With the success of thin-film perovskite solar cells, these absorbers are used as top cells and enabled efficient tandem solar cells with $Cu(In,Ga)Se_2$ [4, 5] or Si as a bottom cell [3, 6].

An advantage of compound thin films is the tunability of the bandgap. For instance, the bandgap of the chalcopyrite family ABC_2, where A, B, and C denote group I, group III, and group IV atom, respectively, can be tuned by alloying on the different atomic sites, for instance by $(Cu,Ag)(In,Ga)(S,Se,Te)_2$. Therefore, it is possible to adapt the bottom cell's bandgap to the values required by the bandgap of the perovskite top cell with highest efficiency and stability. Figure 1 shows a calculation of the theoretical efficiencies for an idealized tandem solar cell either in four-terminal (4T) or two-terminal (2T) configuration as a function of the top- and bottom-cell bandgaps (see Appendix A for details of the calculation). Both architectures allow efficiencies above 45% in the ideal case. The band gap region of high efficiency is larger for the 4T configuration as no current-matching constraints apply. However, the necessity of transparent conductive oxides for the back side of the top cell and the front side of the bottom imposes optical and resistive losses for such a structure, in particular for modules. These losses can be avoided for the 2T architecture. The bottom part in Figure 1 shows the maximum possible efficiency of the tandem

cell as a function of the bottom cell band gap for fixed top cell bandgaps. For the 2T architecture and already indicated by the efficiency map, it is seen that the efficiency of the tandem cell drops quickly for bottom-cell bandgaps away from the optimum. For a top-cell bandgap of 1.6 eV, which is the band gap value of efficient and stable perovskite solar cells [7], the bottom cell's bandgap should be between 0.92 and 0.95 eV. Alloying Ag, Ga, or S to $CuInSe_2$ will only increase the absorbers bandgap above 1.0 eV. However, the $CuIn(Se_{1-x}Te_x)_2$ has a strong bandgap bowing resulting in smallest bandgaps at $x = 0.5$ [8]. Indeed, it is reported that $CuIn(Se_{1-x}Te_x)_2$ can reach bandgap values as low as 0.86 [9] to 0.88 [10] eV for $x = 0.5$ and is thus a suitable candidate for a bottom-cell in a 2T tandem architecture. Also, even with a top-cell bandgap of only 1.5 eV (orange line in Figure 1), the second maximum for the 2T configuration still allows tandem efficiencies of approximately 40%. Noteworthy, also other thin-film material systems are a good match to bottom-cell bandgaps in this energy range. In Ref. [11], a $Cu(In,Ga)S_2$ device with a bandgap of 1.55 eV is demonstrated reaching a single cell power conversion efficiencies of 15.5%. CdTe reaches single cell efficiencies of 22.3% [12], whereas it is noted that these absorber layers are alloyed with Se, which reduces the bandgap outside the optimum range (for top cells in tandem devices) to 1.45 eV.

Noteworthy, the efficiencies calculated in Figure 1 are based on complete absorption for photons with energies larger than the respective bandgaps. Current matching by adapting the top- and bottom-cell bandgaps is the preferred solution because it also leads to a large annual energy yield [13]. In contrast, one of the record $Cu(In,Ga)Se_2$/perovskite tandem uses a perovskite top-cell absorber layer with reduced thickness to achieve current-matching [4]. Thus, the device with full top cell thickness would benefit from a bottom-cell with lower bandgap to achieve current matching in terms of the annual energy yield.

The mixing enthalpy of the $CuIn(Se_{1-x}Te_x)_2$alloy is calculated to be $\Delta H(Se, Te) = 13$ meV/atom and thus indicates phase separation at T = 0 K [8]. However, the phase is stabilized by entropy at finite temperatures, which suggests that the mixed chalcopyrite phase is miscible in the whole compositional range [8]. Experimentally, Avon et al. used sealed quartz capsules and annealed various compositions belonging to the chalcopyrite family $(Cu,Ag)(In,Ga)(Se,Te)_2$ to equilibrium at 600–800 °C [14]. They find that $CuIn(Se_{1-x}Te_x)_2$ is miscible in the complete compositional range. In contrast, Li-Kao et al. used elemental co-evaporation to grow thin films of $CuIn(Se_{1-x}Te_x)_2$ employing either a single-stage or 3-stage process [10, 15]. In the single-stage process, all elements are evaporated with constant fluxes. In contrast, in the three-stage process, the absorber goes from Cu-poor to Cu-rich and subsequently again to Cu-poor composition [16]. To achieve a single-phase absorber layer, it has been found that single-stage absorbers can only be grown up to $x = 0.2$, while three-stage grown absorbers could accommodate a Te content up to $x = 0.4$. Finally, a solar cell has been demonstrated with a bandgap of 0.89 eV with $x = 0.4$ and a power conversion efficiency of 7.0% [15].

Here, we present a detailed study of loss mechanisms of $CuIn(Se_{1-x}Te_x)_2$ absorber layers and solar cells (compared

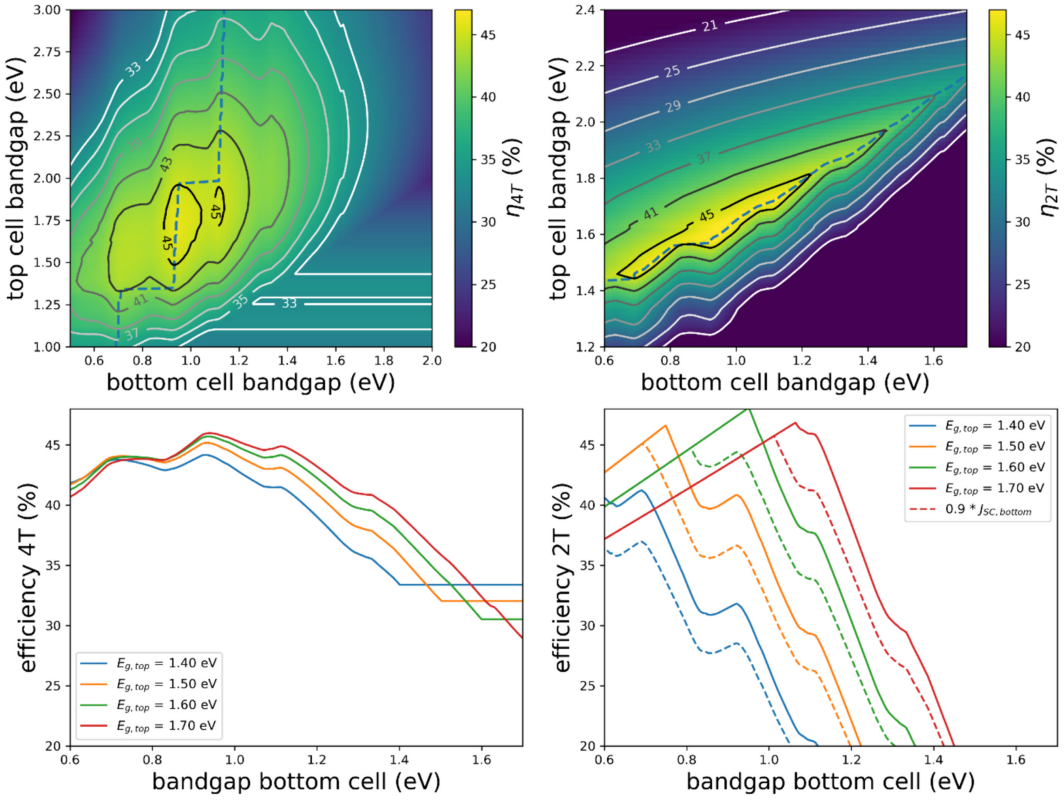

FIGURE 1 | Calculated tandem efficiencies for a four-terminal (left) and a two-terminal (right) configuration as a function of the bandgaps for the top and bottom cell (top). The dashed line in the top maps indicates the optimal choice of the bottom cell bandgap to reach the highest efficiency as a function of the top cell bandgap (or vice versa).

to a reference $CuInSe_2$ sample). We employ a single-stage co-evaporation process and grow absorbers with x up to 0.5. The electronic quality of these absorber layers is characterized by photoluminescence spectroscopy as a function of the Te content. From these absorber layers, solar cells are fabricated and further losses are characterized, which occur upon finishing the absorber layers into solar cells. A solar cell is demonstrated with x = 0.07, a bandgap of 0.97 eV (close to the optimum, see Figure 1) and a power conversion efficiency of 9.0%. This presents the highest efficiency so far of any chalcopyrite with a band gap <1 eV. Finally, performance bottlenecks are pin pointed, which give suggestions for future improvements of these absorber layers and solar cells.

2 | Methods

$CuIn(Se_{1-x}Te_x)_2$ absorber layers are grown by co-evaporation of Cu, In, Se, and Te from elemental sources. Elemental fluxes are changed by adjusting the respective source temperature, which is then kept constant during the deposition, i.e., the absorber layers are grown in a single-stage process. The $CuInSe_2$ absorber layer, which will serve as a reference in this study, is grown using a three-stage process [16]: In the first stage, only In and Se are evaporated. In the second stage, only Cu and Se are evaporated bringing the absorber to a Cu-rich composition, i.e., [Cu]/[In] > 1. In the third stage, again only In and Se are evaporated and a Cu-poor final composition is targeted. Within the same deposition process, absorber layers are grown on soda lime glass (SLG) substrates as well as on SLG/Mo substrates. Substrates are heated radiatively by lamps from the back side. The substrate temperature is set between 550 °C and 570 °C for the samples grown here as measured by thermocouples in close proximity to the backside of the substrates. The deposition time is set between 60 and 80 min. After the deposition of the absorber layers, the samples are cooled down naturally with a maximum cooling rate of 30 °C/min. During cooldown, Te and Se evaporation is continued. Evaporation of Te is stopped at a substrate temperature of 400 °C. At 250 °C, the samples are taken out of the evaporation chamber into the loadlock, which effectively stopped the Se evaporation at 250 °C.

Composition is measured by energy dispersive X-ray analysis in an electron microscope using elemental standards. The acceleration voltage is set to 20 kV. Generally, samples with transparent SLG substrates have a higher Te content than the samples with Mo back contact from the same process run. The reason might be a lower substrate temperature due to lower absorption of the radiation from the substrate heater.

Structural analysis is carried out by X-ray diffraction (XRD) in Bragg–Brentano configuration with 2Θ ranging from 10° to 90° with a step-size of 0.02°.

One sample was analyzed by SIMS, using a CAMECA SC-Ultra with Cs^+ ions at 1 keV in MCs_x^+ mode, where M are the elements of interest.

An approximately 40 nm thick CdS buffer layer is grown by chemical bath deposition. Prior to buffer deposition, the absorber layers are etched in 5 wt. % potassium cyanide (KCN) for 30 s to remove oxide layers and clean the surface.

Photoluminescence (PL) spectroscopy is carried out in a self-built setup on absorber/buffer stacks, i.e., without deposition of a window layer and thus without the introduction of a space charge region. A 660 nm diode laser is used as excitation source. The PL flux is collected by two off-axis parabolic mirrors and directed via an optical fiber into a monochromator. A grating is used to disperse the PL light onto a 512 element InGaAs detector array. The excitation flux as well as the PL flux is calibrated to absolute photon numbers as described elsewhere [17]. Some of the PL spectra are influenced by interference fringes. In that case, the PL peak position is estimated using a Gaussian fit in a range that is less influenced by interference fringes. Supplementary Figure S1 shows the procedure in the presence (a) or absence (b) of interference fringes in the PL spectrum. This approach is not without uncertainty concerning the peak position but allows to analyze a large number of samples. Some of the scatter in the data, e.g., in Figure 4, might be due to this approach.

The quasi-Fermi level splitting (QFLS) can be determined from a fit to the high-energy slope of the PL spectrum to Planck's generalized law, assuming that the absorptance is close to 1 in that energy range [18]. We fit keeping the temperature equal to the measured temperature during the PL measurement, as discussed in [19]. It has been shown that the energy range well above the band gap, where absorptance is nearly complete, is not affected by interferences [20].

The optical diode factor is measured on some samples using excitation dependent PL using Equation (1) [21, 22].

$$A = \frac{\partial \ln \Phi_{PL}}{\partial \ln G} \tag{1}$$

where Φ_{PL} is the spectrally integrated PL flux and G is the generation flux. As for the spectral PL measurements, these measurements are carried out on absorber/buffer stacks. As no space charge region is present, the optical diode factor corresponds to the diode factor of the quasi-neutral region.

Time-resolved PL is recorded with a time-correlated single photon counting unit. The sample is excited with a pulsed laser at 10 MHz repetition rate and a wavelength of 640 nm.

Solar cells are finished from the absorber/buffer stacks by sputtering a transparent conductive oxide consisting of a double layer of i:ZnO/Al:ZnO. Subsequently, a Ni/Al grid is deposited by e-beam evaporation. Two cells have received an additional MgF_2 layer, prepared by electron beam deposition, as anti-reflective coating (ARC).

For each sample, six solar cells are defined by mechanical scribing areas of approximately 0.5 cm^2. Exact areas are determined using a microscope coupled to a digital camera. Parameters of the individual solar cells in this paper are shown only for the solar cells, which have an efficiency of at least 70% of the efficiency of the best solar cell on the same substrate.

Current density voltage (JV) characteristics are measured under an AAA solar simulator at standard test conditions. JV data is fitted following a 1-diode model (Equation (2)), where the orthogonal distances are minimized on a logarithmic ordinate axis.

$$J(V) = J_0 \left[\exp\left(\frac{q(V - r_s J)}{A_{el} k_B T} \right) - 1 \right] + \frac{V - r_s J}{R_{sh}} + J_{ph} \quad (2)$$

In Equation (2), J is the current density, V the applied bias voltage, J_0 is the saturation current density, A_{el} the electrical diode factor, r_s the series resistance, R_{sh} the shunt resistance, J_{ph} the photo-current, k_B the Boltzmann constant, q the elemental charge, and T the temperature.

The external quantum efficiency (EQE) is measured in a self-built setup with a lock-in amplifier. No bias voltage or bias light is applied during the measurements. Calibrated Si and InGaAs photodiodes are used as a reference. The photovoltaic bandgap $E_{G,PV}$ is determined from the $dEQE/dE$ peak as suggested by Rau et al. [23]. However, for a number of samples in this study, the EQE is influenced by interference fringes near the absorption edge, which prevents a straight forward application of the procedure to obtain $E_{G,PV}$.Therefore, similar as for the determination of the PL peak position, the $dEQE/dE$ spectra are fitted with a Gaussian curve and the maximum is used for $E_{G,PV}$. Supplementary Figure S1 shows examples of the determination of the $dEQE/dE$ peak position in the absence (a) or presence (b) of interference fringes in the EQE spectrum.

Capacitance-voltage (CV) measurements are carried out in the dark at 300 K, using an ac-modulation voltage of 30 mV. The sample is kept in the dark over night at 300 K before the measurement, so that a relaxed state is obtained.

Transmittance T and reflectance R spectra are acquired in a photospectrometer using an integrating sphere. The absorption coefficient α is calculated taking into account reflections from a freestanding film [24–26], from which the direct bandgap $E_{g,dir}$ is determined from a Tauc plot following Equation (3) [27].

$$\alpha E \propto \sqrt{E - E_{g,dir}} \quad (3)$$

where E is the photon energy.

3 | Results

Figure 2 shows X-ray diffractograms of the 1 1 2 reflection of various $CuIn(Se_{1-x}Te_x)_2$ absorber layers with different compositions x. With increasing Te content, the 1 1 2 reflection shifts towards smaller 2Θ values. This is expected due to the larger atomic size of Te compared to Se and thus increased lattice constants [14]. There is no indication of additional phases for the complete investigated compositional space, indicating that it is possible to achieve single-phase material. This is further evidenced by rather narrow 1 1 2 reflections. Furthermore, we observe a monotonous shift of 1 1 2 reflection with increasing Te

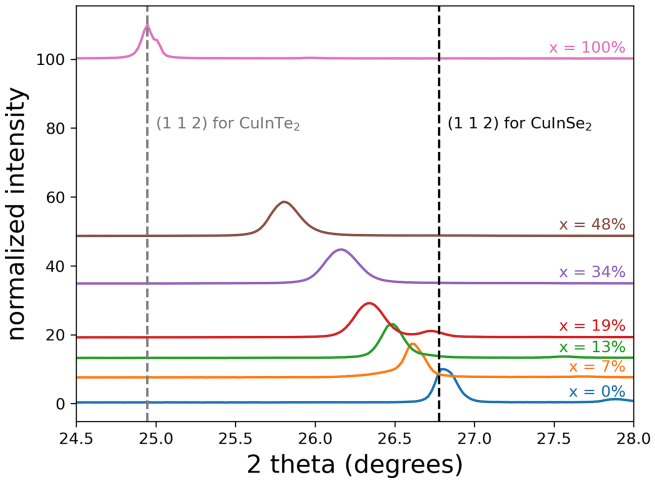

FIGURE 2 | X-ray diffractograms of the 1 1 2 reflection of $CuIn(Se_{1-x}Te_x)_2$ absorber layers — shifted vertically in proportion to the Te content for clarity. Vertical black and gray line indicates the position of the 1 1 2 reflection for the $CuInSe_2$ and $CuInTe_2$ film, respectively.

content, indicative of a homogeneous main phase with increasing lattice constant. Elemental depth profiles are obtained from SIMS data. Supplementary Figure S3 shows the profiles for Cu, In, Se, and Te, which are fairly flat throughout the depth of the $CuIn(Se_{1-x}Te_x)_2$ film in agreement with the narrow 1 1 2 reflections. These results show that there is no indication of a miscibility gap in $CuIn(Se_{1-x}Te_x)_2$ at least up to x = 0.5, which is the relevant compositional range for applications as a bottom-cell. In addition, it is possible to grow single-phase $CuIn(Se_{1-x}Te_x)_2$ up to at least x = 0.5 using a single-stage process, unlike reported previously where x = 0.2 was given as a limit [15].

Photoluminescence spectroscopy is carried out to investigate the opto-electronic quality of absorber layers before forming the pn-junction. Only a CdS buffer layer is deposited on top of the absorber layer for surface passivation [28, 29]. The PL peak position reflects the energy of the band-to-band transition and is, thus, an indicator of the bandgap of the absorber layer, albeit slightly underestimating the true band gap [30]. In addition, QFLS is determined using Planck's generalized law from the high energy slope of the PL peak [18, 19], which represents an upper limit for the open circuit voltage V_{OC}. Figure 3 shows normalized PL spectra of selected absorber layers with different compositional values x. Clearly, the PL spectra shift towards lower energies with increasing Te content in the absorber layer in the considered composition range. This red shift can be linked to a lowering of the bandgap, as expected upon alloying $CuInSe_2$ with Te [9, 10]. Furthermore, there is no significant broadening of the PL spectra with the addition of Te. The x = 19% sample shows even narrower PL than the $CuInSe_2$ sample. This observation indicates that there is no additional broadening in the band gap distribution and supports the miscibility in this composition range.

Another observation is that the PL spectra exhibit multiple peaks, which is strongest pronounced for the sample with x = 7% in Figure 3. These multiple peaks are not necessarily different phases or defect related transitions, but can be

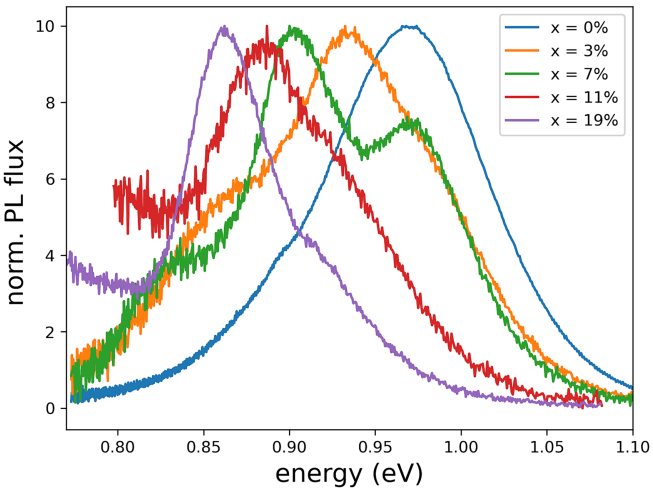

FIGURE 3 | Normalised PL spectra of selected $CuIn(Se_{1-x},Te_x)_2$ absorber layers with different composition x.

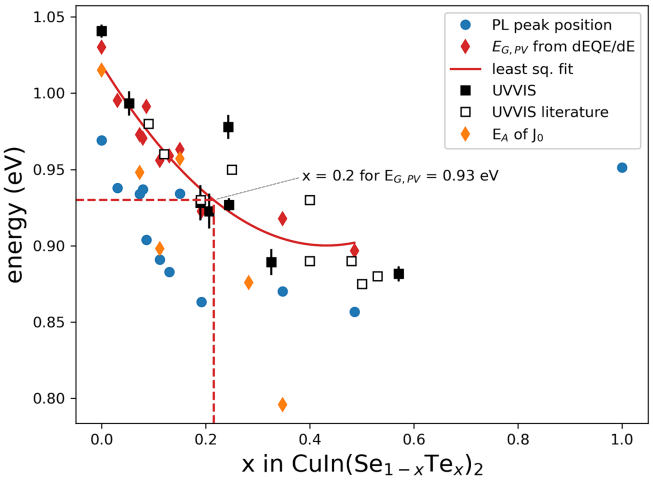

FIGURE 4 | Estimations of the bandgap energy as a function of the Te content x. The red curve describes a least square fit to the band gap values.

caused by interference effects [31]. In order to check if interference effects are the root of these multiple peaks, reflectance spectra are measured on the exact same samples. The PL and the reflectance spectra are both plotted in Supplementary Figure S1. It is shown that the PL peak positions are in good agreement with the peak positions of the reflectance. To support the hypothesis of interference effects, PL spectra are acquired with the sample tilted with respect to the laser beam and thus the direction of PL collection (i.e., not perpendicular). For such a modification of the sample orientation, the effective optical path of the PL light increases. Therefore, the interference fringes are expected to change as a function of the sample tilt angle [32]. Supplementary Figure S2 shows the PL spectra at two different tilt angles for a sample, which is strongly influenced by interference fringes in standard measurement configuration (excitation and collection perpendicular to the absorber's surface). It is shown that the PL peaks shift when tilting the sample, which is a strong support for the hypothesis that the different PL peaks are caused by interference fringes. Thus, in order to estimate the PL energy for the band-to-band transition, i.e., the peak position, which would be obtained if interference fringes were absent or less pronounced, a Gaussian fit is carried out as detailed in Section 2 (methods) and exemplarily shown in Supplementary Figure S1. For a larger set of samples, the PL peak positions from such a Gaussian fit are plotted versus the Te content x in Figure 4 as blue circles. The PL peak position decreases up to $x \approx 0.5$. For $x = 1$, i.e., $CuInTe_2$, the PL peak position is similar to the one of $CuInSe_2$. The reason is the strong bowing for the bandgap of $CuIn(Se_{1-x}Te_x)_2$ [8].

The bandgap is also determined from transmittance and reflectance data obtained by spectrophotometry for samples grown on SLG substrates without a Mo back contact, i.e., on transparent substrates. The extracted bandgap values are shown in Figure 4 as black squares. As for the PL peak position, a decreasing bandgap with increasing Te content up to $x \approx 0.5$ is observed. However, the bandgap values determined from spectrophotometry are roughly 50 meV higher than the PL peak positions. The reason for the red-shifted PL peak positions from their bandgap values can be explained by tail states [30, 33]. In particular, it is shown in [33] that the emitted photon spectrum is red-shifted compared to the absorptance spectrum, which explains the 50 meV difference observed here. It is interesting to note that the energetic distance between bandgap and PL maximum does not increase with the addition of Te, indicating no increase in the tail states or no broadening of the band gap distribution, further supporting miscibility.

Bandgap values $E_{G,PV}$ of the photovoltaic devices are determined by EQE measurements as described in Section 2 (methods) and are plotted as red diamonds in Figure 4. These bandgap values are in good agreement with the values determined by spectrophotometry. This behavior is expected, as the EQE is determined by the absorptance spectrum of the thin film solar cell. Bandgap values from literature [10, 15] (determined from transmittance and reflectance measurements and the Tauc plot) are plotted as open squares and agree with the values reported here.

JV characteristics are measured for all solar cell devices with different compositions x. The V_{OC}'s are plotted versus x in Figure 5 as blue circles. Plots of the efficiency, J_{SC}, fill factor, and extracted diode factor are shown in Supplementary Figure S5. The highest V_{OC} of 462 mV is obtained for a $CuInSe_2$ device grown in the same deposition machine. Using the fitted values of $E_{G,PV}$ (red line in Figure 4), expected V_{OC} values are shown in Figure 5 as a red dashed line under the assumption of the same luminescence quantum efficiency (PLQY) Y_{PL} in the $CuIn(Se_{1-x}Te_x)_2$ devices as in our $CuInSe_2$ device, i.e., we use $V_{OC} = V_{OC}^{SQ}(E_G) + kT\,ln\,Y_{PL}$ with V_{OC}^{SQ} the Shockley–Queisser V_{OC} for the given band gap (as taken from the fitted values from Figure 4). We neglect the change in $E_G - V_{OC}^{SQ}$, which is justified by the small change in E_G. Furthermore, this approach neglects the short circuit and the radiative V_{OC} losses, because it has been shown that the non-radiative loss due to Y_{PL} is by far the most important loss [23]. Clearly, V_{OC} drops below the expectation as soon as Te is alloyed to $CuInSe_2$. Upon incorporation of Te, V_{OC} drops below 400 mV. For $x \approx 0.5$, V_{OC} drops below 200 mV. The black dashed line is a polynomial fit of

order two to the best V_{OC} values of all samples alloyed with Te. Thus, the red area indicates additional non-radiative losses in the solar cells that occur when Te is incorporated.

In contrast, QFLS values obtained from absolute PL measurements (orange diamonds in Figure 5) are closer to the red curve, i.e., the curve with no new additional non-radiative losses, in particular for samples with x > 0.25. The QFLS losses (Equation 4) and V_{OC} losses (Equation 5) allow a closer inspection of non-radiative losses as a function of Te content in the absorber.

$$QFLS\ \text{loss} = E_g - QFLS \tag{4}$$

$$V_{OC}\ \text{loss} = E_g - V_{OC} \tag{5}$$

Smaller values of these loss quantities indicate a lower fraction of non-radiative recombination and thus a superior electronic material quality. Figure 6 shows the QFLS and V_{OC} losses using $E_{G,PV}$ or the PL peak position as the bandgap value E_g in Equations (4) and (5). The QFLS losses (Figure 6a) scatter by up to 100 meV; however, no clear trend with the Te content x is observed. In particular, various samples exist with similar or even lower QFLS losses compared to the reference sample with x = 0. This indicates that the electronic quality of the absorber bulk does not deteriorate and can even improve with the incorporation of Te.[1]

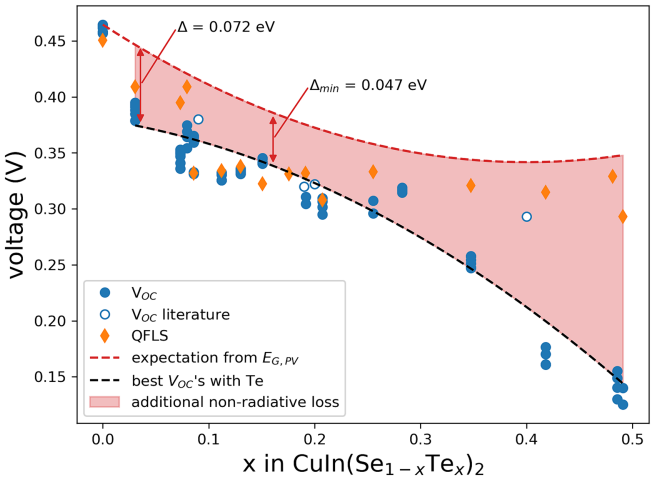

FIGURE 5 | Open circuit voltages (blue circles) and quasi Fermi level splittings (orange diamonds) for $CuIn(Se_{1-x}Te_x)_2$ devices and absorber layers. The red dashed curve shows the expected decrease of the V_{OC} upon Te incorporation into $CuInSe_2$ based on the fitted bandgap values $E_{G,PV}$ (see Figure 4), assuming the same PLQY. Black dashed line is a least square fit of a polynomial with order 2 to the best V_{OC} values for each sample, which serves as a guide to the eye for V_{OC} as a function of x. Literature data for $V_{OC}(x)$ is taken from [10, 15].

In contrast to the QFLS losses, V_{OC} losses (Figure 6b) have the lowest value for $x = 0$, i.e., for $CuInSe_2$. Therefore, we can conclude that additional non-radiative losses are introduced upon finishing the absorber to a solar cell. The increasing difference between QFLS and V_{OC} indicates the occurrence of interface recombination [34]: interface recombination leads to a gradient in minority quasi-Fermi level and thus to a lower V_{OC} than the QFLS. A few samples are measured using temperature dependent IV (IVT) to determine the activation energy of the saturation current J_0 from $E_A = qV_{OC}(T = 0)$, which is obtained from extrapolation of $V_{OC}(T)$ to $T = 0$ (orange symbols in Figure 4) [35]. For some samples, E_A matches well the respective bandgap value $E_{G,PV}$. For two other samples, E_A is slightly reduced compared to $E_{G,PV}$ with $E_{G,PV} - E_A \approx 50$ meV. However, the sample with the highest Te content measured by IVT with x = 34% shows a significantly reduced E_A. Supplementary Figure S6 shows a correlation of $QFLS - V_{OC}$ versus $E_{G,PV} - E_A$ and supports the claim that additional non-radiative recombination channels at the $CuIn(Se_{1-x}Te_x)_2$/CdS interface are introduced upon finishing the absorber to a solar cell.

It is interesting to note that a solar cell with $x = 0.4$ and $V_{OC} = 0.293$ V is presented in ref. [15]. In particular, the V_{OC} is ≈ 80 mV higher than the interpolation of our best V_{OC} values (black dashed line) and thus has a relatively small V_{OC} loss considering a Te content of x = 0.4 (Figure 6b). The V_{OC} value is however similar to the QFLS values we obtain in this compositional range. The device structure for the devices reported in [15] is the same as used in this study. However, a distinct difference in the growth process of the absorber layer is the utilization of a three-stage process [16] in ref. [15]. How a three-stage process influences the interface properties and thus avoids the addition of recombination channels upon finishing the solar cell is unclear at the moment and remains to be investigated.

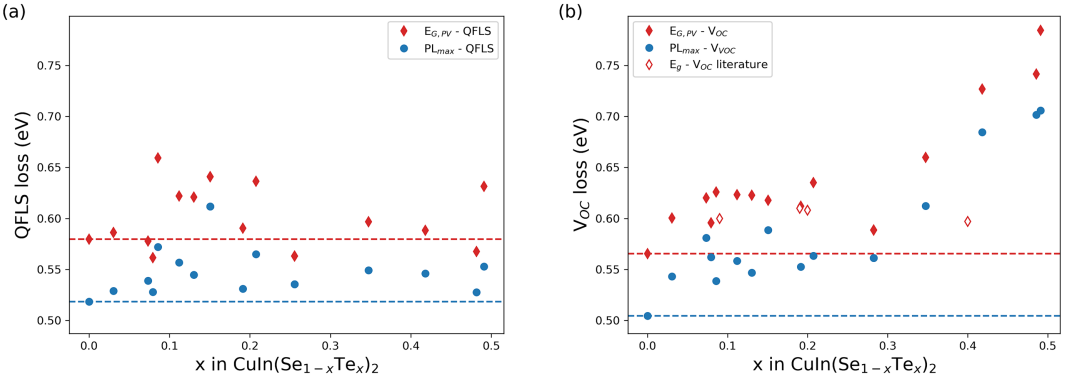

FIGURE 6 | QFLS losses (a) and V_{OC} losses (b) for $CuIn(Se_{1-x}Te_x)_2$ absorber layers and solar cells as a function of composition x. Horizontal dashed lines indicate the respective loss-value for $x = 0$. Literature data is taken from refs. [10, 15], where the bandgap is determined from spectrophotometry and a Tauc plot.

Representative JV characteristics and EQE spectra of the best solar cells are shown in Figure 7. The extracted parameters for the performance of the JV curves are listed in Table 1. As already shown in Figure 5, V_{OC} drops upon Te alloying. EQE measurements of samples with increasing Te content show a response towards larger wavelengths due to the lowered bandgaps for these solar cells. However, the photo-current is not enhanced by the wider spectral range, because of the lowered EQE values across most of the spectrum. The drop in EQE for wavelengths $\gtrsim$ 900 nm can be attributed to incomplete carrier collection. This reduced collection may be caused at least in part by a shorter space charge region due to higher doping of Te containing samples (see Figure 8). For a use of these solar cells as bottom cells in tandem devices, in particular the long wavelengths response is important. It should be noted that even the reference $CuInSe_2$ device shows a reduced EQE beyond 900 nm. This device was prepared in the same machine by a more optimized but obviously not perfect process. $CuInSe_2$ devices have shown much better EQE up to 1200 nm (see e.g. [36, 37]), therefore, it seems a matter of absorber optimization, mostly in terms of doping level, to improve the EQE and the short circuit current. Losses at shorter wavelengths are probably caused by additional recombination channels for Te containing solar cells in agreement with the larger V_{OC} loss (Figure 6b). It is noted that the baseline sample with $x = 0$ does not have an ARC. Hence, losses in EQE are dominated by reflection losses, which is not the case for the two samples with an ARC with $x = 7$ % and $x = 15$ %. The solar cell with x = 0.07 and a band gap of 0.97 eV shows an efficiency of 9.0%, the highest efficiency for a $CuIn(Se_{1-x}Te_x)_2$ device so far.

It is encouraging that the QFLS loss is not deteriorating when alloying $CuInSe_2$ with Te (Figure 6a). However, for a doped (p-type for $CuInSe_2$ polycrystalline films) semiconductor, the QFLS can be modified by a change of the doping density or the minority carrier lifetime. The doping density is determined on solar cells from capacitance-voltage measurements as described in the methods section. The doping profiles as a function of voltage are shown in Supplementary Figure S7. The evaluated minimum of the apparent doping density is plotted as a function of the Te content x in Figure 8. The apparent doping density increases by roughly one order of magnitude from $\approx 4 \times 10^{15}$ cm^{-3} for x = 0 to $\approx 5 \times 10^{16}$ cm^{-3} for x = 0.26. Such an increase in the doping density would increase the quasi-Fermi level splitting by approximately 60 mV [19, 38], which however is not observed. A possibility is a deterioration of the minority carrier lifetime such that the quasi Fermi level splitting does not increase with increasing Te content.

To estimate the minority carrier lifetime, time resolved PL measurements are carried out. Experimental PL transients for absorbers with various compositions x are shown in Figure 9a as semi-transparent lines. The $CuInSe_2$ sample shows a minor initial drop of PL intensity and subsequently follows a single-exponential behavior around 3 ns after the laser pulse. Such a single-exponential behavior is expected for a p-type absorber in low-injection conditions [39]. The initial non-exponential drop might be due to high injection conditions near the absorber's surface just after the injection pulse and/or due to surface recombination. Samples that are alloyed with Te show a much

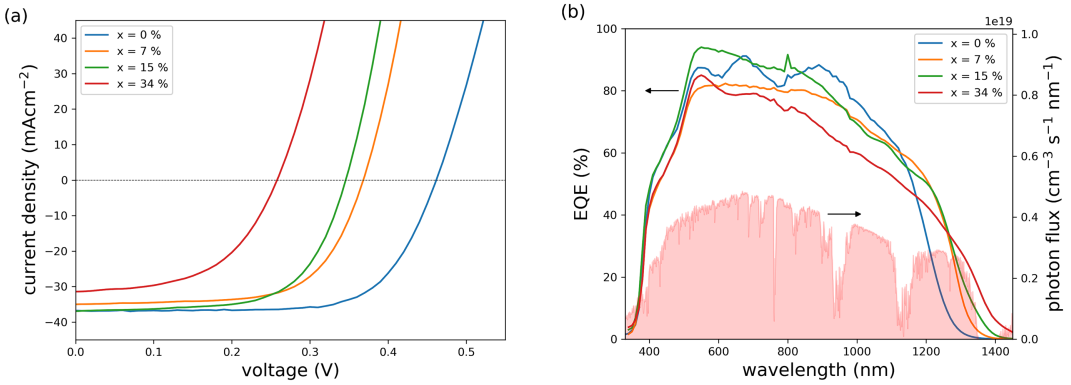

FIGURE 7 | a) Best IV characteristics for the $CuInSe_2$ reference (x = 0) and with Te alloyed solar cells. b) EQE spectra for the same cells as shown in a). Shaded red area on right ordinate shows the photon flux of the AM1.5G spectrum. Note, that the solar cells with x = 7% and x = 15% have an anti-reflective coating.

TABLE 1 | Parameters of the IV characteristics shown in Figure 7.

Composition x (%)	V_{OC} (mV)	J_{SC} (mAcm^{-2})	*FF* (%)	Efficiency (%)	$E_{G,PV}$ (eV)
0	462	36.9	70	11.9	1.03
7[a]	374	36.1	67	9.0	0.97
15[a]	341	37.4	65	8.2	0.96
34	257	31.4	53	4.3	0.92

[a]With anti-reflective coating.

more pronounced initial drop compared to the $CuInSe_2$ absorber and go into a single-exponential behavior roughly 10 ns after the laser pulse. To estimate the tail lifetime (single exponential decay after approximately 10 ns after the pulse) and the magnitude of the initial drop in PL intensity, the transients are fitted with a double exponential function:

$$PL(t) = A_1 \exp\left(-\frac{t}{\tau_1}\right) + A_2 \exp\left(-\frac{t}{\tau_2}\right) \quad (6)$$

In Equation (6), A_1 and A_2 are the prefactors or amplitudes of the exponential functions and τ_1 and τ_2 the respective lifetimes. Fits to Equation (6) are shown as solid lines in Figure 9a and the fit values τ_2 and A_2 for the second exponential are shown in Figure 9b and c, respectively. Only fit values for the second exponential are shown due to several reasons:

i. The second exponential describes the tail lifetime and thus can be identified as the effective lifetime of the minority carriers [40, 41]. Note that this lifetime includes effects of bulk and interface recombination.

ii. The initial drop can have various reasons such as: high injection conditions and a subsequent reduction in PL intensity due to reduced bi-molecular recombination and diffusion of charge carriers [42]; minority carrier trapping [43]; space charge regions, which separate charge carriers [44]; enhanced front-surface recombination [42]

Nevertheless, the first exponential is included in the fit (except for the $CuInSe_2$ sample) in order to disentangle the two contributions and to obtain more reliable parameters for the second exponential. The full set of fit parameters is presented in Supplementary Figure S9.

It is observed that the effective lifetime decreases from 22.5 ns for our $CuInSe_2$ sample to approximately 10–12 ns for $x > 0$ independent of the Te content (Figure 9b). The amplitude of the second exponential however decreases significantly the higher the Te content in the absorber (Figure 9c). These two phenomena are apparent in Figure 9a as the transients are all more or less parallel for t > 10 ns, but shifted vertically, due to a larger initial drop for higher Te contents. The drop of the effective minority carrier lifetime by a factor of approximately two implies a drop in the QFLS by roughly 20 meV [19].

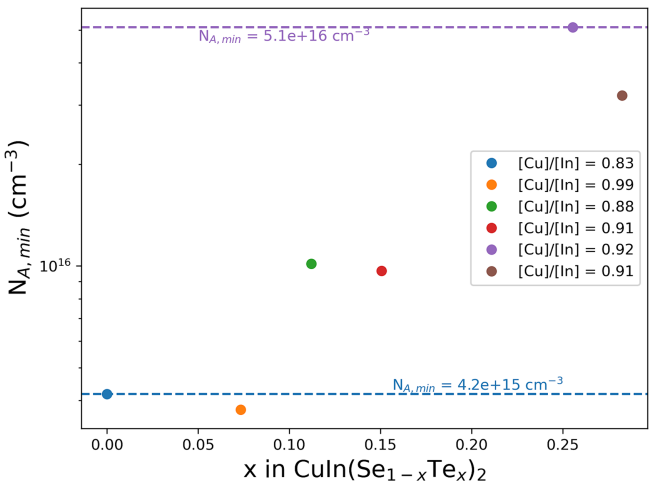

FIGURE 8 | Apparent doping density obtained from C(V) measurements carried out at 300 K in the relaxed state. Except the sample with almost stochiometric [Cu]/[In] ratio, the apparent doping density seems to increase by almost one order of magnitude when adding Te with $x = 0.25$ to $CuInSe_2$.

Thus, from the increase in doping, we expect a decrease of the QFLS loss by about 60 meV and from the decrease in life, an increase in QFLS loss of about 20 meV. Together, we would expect an improvement of 40 meV in QFLS relative to the band gap, which is not observed (Figure 5).

4 | Discussion

While an efficiency of 8 to 9% with a bandgap around 0.96 eV is an encouraging result, it is far from what is needed for a bottom cell in a tandem device. All solar cell parameters fall short of the expectations. Here we give a detailed analysis of the losses and discuss potential solutions. In Section 3, already several losses for $CuIn(Se_{1-x}Te_x)_2$ solar cells are presented and compared to a $CuInSe_2$ reference device. Interestingly, the QFLS is deteriorating very little when introducing Te into the absorber layer as seen in Figure 6a. However, the doping density increases and the minority carrier lifetime decreases with incorporation of Te. The combined effect of these two quantities would imply an increased QFLS relative to the band gap by 40 meV, or the QFLS loss would decrease by 40 meV with the addition of Te. However, this is not observed. A possibility might be that the minority carrier lifetime is influenced by trapping [43] or space-charge region effects [44] and is, thus, overestimated. Both effects can also explain an increased non-exponential initial drop of the PL signal, i.e., the decrease in the amplitude of the second exponential (Figure 9c). Importantly, the increase of the initial drop is not caused by high-injection conditions, as the doping density increases with Te content (Figure 8), which would rather decrease the range where high injection condition prevail to shorter times. Thus, it is possible that the extracted effective minority carrier lifetimes (Figure 9b) are overestimated (due to trapping or space-charge regions), which might be the reason why the QFLS loss is not decreasing with Te content. Additionally, a true minority carrier lifetime smaller than shown in Figure 9b could explain the drop in EQE at long wavelengths due to incomplete collection shown in Figure 7b.

Noteworthy, a pure $CuInTe_2$ absorber without Se is also investigated by PL and shows a QFLS of 456 meV, similar to the value of our $CuInSe_2$ absorber (451 meV). However, neither a PL transient with a response above the instrumental response function (~400 ps) could be measured, nor a functioning device could be fabricated from this absorber layer. We believe that the doping increases significantly for the $CuInTe_2$ absorber, which enables such higher QFLS, while the minority carrier lifetime decreases accordingly. This hypothesis is in agreement with the discussion above.

Next, we focus on the composition of $x = 0.2$ for a bandgap of 0.93 eV. The doping density is around 2×10^{16} cm^{-3} based on Figure 8 and thus well suited for a photovoltaic device. It is

known that the doping in Cu(In,Ga)Se_2 is metastable and that doping densities in the order of $10^{16}\,cm^{-3}$ are achieved after light soaking [45, 46], i.e., in operating conditions. Recently, it was shown that this metastable doping density is responsible for an increased diode factor and therefore a reduced fill factor [46, 47]. However, in case of a larger fixed (non-metastable) doping density, a smaller diode factor is expected [46, 48]. For the CuIn $(Se_{1-x}Te_x)_2$ solar cells presented here, the relaxed doping density is already in the order of $10^{16}\,cm^{-3}$ and thus a smaller diode factor due to metastability is expected. Indeed, measurements of the optical diode factor on absorber/buffer stacks, i.e., without a space charge region, yield values between 1.1 and 1.2 (Supplementary Figure S8). These values of the diode factor represent the diode factor in the quasi neutral region. Due to the higher doping density, these diode factors are smaller than the ones generally obtained for Cu(In,Ga)Se_2 absorbers around 1.3 [22, 47]. This is an important finding because the doping density is less influenced by metastabilities. Thus, solar cells can be realized with low diode factors and therefore relatively large fill factors. For the devices presented here, however, the electrical diode factors (i.e., obtained from the JV characteristics) do not improve significantly (Supplementary Figure S5). Potential reasons might be a decreased inversion in combination with interface recombination, or the addition of SCR recombination.

While the QFLS loss can be maintained, the V_{OC} loss increases with Te content (Figure 6b). The constant QFLS loss indicates that the addition of Te does not introduce any additional non-radiative recombination paths in the bulk of the absorbers. IVT measurements and the determination of E_A of J_0 indicate that additional non-radiative recombination is introduced at the CuIn$(Se_{1-x}Te_x)_2$/CdS interface. Based on density functional theory calculations, Zunger and Wei predicted that the conduction band minimum of $CuInTe_2$ is 0.47 eV higher than the one of $CuInSe_2$ [8]. Thus, it is possible that a cliff-like band-alignment at the absorber/buffer interface is introduced by alloying $CuInSe_2$ with Te. This cliff might be more pronounced for higher Te contents, which is also indicated by the increase in $E_{G,PV} - E_A$ (Supplementary Figure S6). The effect of an enhanced interface recombination, caused by the cliff-like band alignment, is always stronger reflected in the V_{OC} loss than in the QFLS loss, because it causes gradients in the minority quasi-Fermi level [34]. In addition, the higher doping density with Te content reduces inversion of the interface and may enhance front interface recombination [49]. Since alloying with Te also shifts the valence band up [8], we need to consider increased recombination at the back contact, as well. However, already in the reference cell the back contact is an unpassivated Mo metal contact with high recombination velocity (around 10^6 cm/s) [41]. Backside recombination cannot get much worse. Furthermore, any significant increase in backside recombination would also reduce QLFS, since PL is measured at absorbers on the back contact. We observe no increase in the QFLS loss (Figure 6a), therefore we exclude a significant increase of the backside recombination. On the other hand, a higher valence band edge compared to $CuInSe_2$ could lead to a barrier for the whole transport under forward

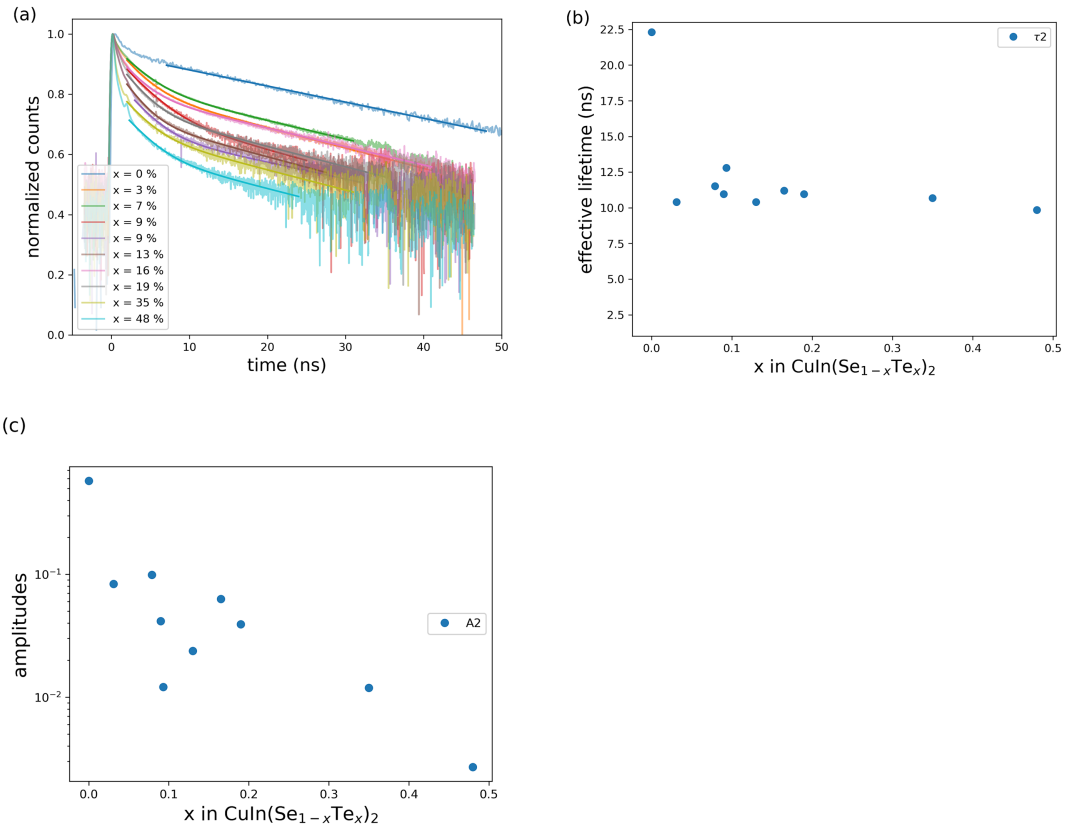

FIGURE 9 | a) Experimental PL transients for various Te contents x plotted as semi-transparent lines. Double exponential fits are shown as solid lines. b) Tail lifetime τ_2 of the second exponential as a function of x. c) Amplitude of the second exponential as a function of x.

bias. Since we do not observe kinks in the IV characteristics (Figure 7a), we have no indication of a significant hole barrier at the back contact. The reduction of the fill factor with increase Te content could be a hint for an increasing barrier, but it could have also many other reasons in these non-optimized solar cells.

Thus, in order to obtain high efficiency CuIn $(Se_{1-x}Te_x)_2$/buffer stacks, it is advised to investigate different buffer layers with higher conduction band minima such as (Zn,Sn)O [50, 51] or (Zn,Mg)O [52].

In addition, it is worthwhile to study how to control the doping density in these absorber layers, which will be critical to improve the EQE at long wavelengths. In particular, for 2 T tandem applications, a good collection of charge carriers is of importance so that no current-mismatch occurs. Likely, the amount of Na and the Cu content need to be better controlled to obtain an optimum doping level and improve both charge carrier collection and V_{OC}.

5 | Conclusion

$CuIn(Se_{1-x}Te_x)_2$ absorber layers are fabricated by co-evaporation from elemental sources. Bandgap values as low as 0.9 eV (determined from EQE measurements) are possible for a composition of $x = 0.5$. The QFLS loss, i.e., $E_g - QFLS$, can be maintained upon alloying $CuInSe_2$ with Te, indicating no addition of non-radiative recombination channels. However, the doping density increases, while TRPL measurements indicate a reduction of the effective minority carrier lifetime, i.e., the combined recombination caused by bulk and surface recombination. In contrast to the QFLS loss, the V_{OC} loss increases with the addition of Te, indicating interface recombination. Dominating interface recombination is also indicated by the activation energy of J_0 from temperature dependent JV measurements. To avoid the V_{OC} loss with Te incorporation, it is important to optimize the absorber/buffer interface. In particular, it seems that a cliff-like band alignment to the CdS buffer prevails and is responsible for V_{OC} losses for a sufficiently large Te content in the absorber ($x \gtrsim 0.3$). We believe that alternative buffer layers such as (Zn,Sn)O will enable higher efficiencies for low bandgap absorbers. These absorber layers will then enable an additional degree of freedom for the design of tandem solar cells.

Acknowledgments

Michele Melchiorre and Thomas Schuler are acknowledged for technical assistance. We thank Nathalie Valle and Brahime El Adib from Luxembourg Institute of Science and Technology for the SIMS measurement. For the purpose of open access, the authors have applied a Creative Commons Attribution 4.0 International (CC BY 4.0) license to any Author Accepted Manuscript version arising from this submission.

Conflicts of Interest

The authors declare no conflicts of interest.

Data Availability Statement

The data presented in this paper is available on zenodo.org (https://zenodo.org/records/10492613).

Endnote

[1] Looking at Figure 5 at the red dashed line and the values of the QFLS, it might be surprising that some samples show a smaller QFLS loss (Figure 6a) than the $CuInSe_2$ sample. However, for the data points in Figure 6b, the actual measurements of $E_{G,PV}$ (red diamonds in Figure 4) are used, not the interpolated values.

References

1. E. G. Hertwich, J. Aloisi de Larderel, A. Arvesen, et al., *Green Energy Choices: The Benefits, Risks and Trade-Offs of Low-Carbon Technologies for Electricity Production* (New York: United Nation's Environment Programme, 2016), 2016.

2. W. Shockley and H. J. Queisser, "Detailed Balance Limit of Efficiency ofp-nJunction Solar Cells," *Journal of Applied Physics* 32 (1961): 510–519.

3. M. A. Green, E. D. Dunlop, M. Yoshita, et al., "Solar Cell Efficiency Tables (Version 62)," *Progress in Photovoltaics: Research and Applications* 31 (2023): 651–663.

4. M. Jošt, E. Köhnen, A. Al-Ashouri, et al., "Perovskite/CIGS Tandem Solar Cells: From Certified 24.2% Toward 30% and Beyond," *ACS Energy Letters* 7 (2022): 1298–1307.

5. T. Feeney, I. M. Hossain, S. Gharibzadeh, et al., "Four-Terminal Perovskite/Copper Indium Gallium Selenide Tandem Solar Cells: Unveiling the Path to >27% in Power Conversion Efficiency," *Solar RRL* 6 (2022): 2200662.

6. https://www.kaust.edu.sa/en/news/kaust-team-sets-world-record-for-tandem-solar-cell-efficiency.

7. T. C. J. Yang, P. Fiala, Q. Jeangros, and C. Ballif, "High-Bandgap Perovskite Materials for Multijunction Solar Cells," *Joule* 2 (2018): 1421–1436.

8. A. Zunger and S.-H. Wei, "Electronic Structure Theory of Chalcopyrite Alloys, Interfaces, and Ordered Vacancy Compounds," *AIP Conference Proceedings* 353 (1996): 155–160.

9. R. Diaz, M. León, and F. Rueda, "Characterization of Cu-In-Se-Te System in Thin Films Grown by Thermal Evaporation," *Journal of Vacuum Science & Technology, A: Vacuum, Surfaces, and Films* 10 (1992): 295–300.

10. Z. Jehl-Li-Kao, T. Kobayashi, and T. Nakada, "CuIn(Se1−xTex)2 Solar Cells With Tunable Narrow-Bandgap for Bottom Cell Application in Multijunction Photovoltaic Devices," *Solar Energy Materials and Solar Cells* 119 (2013): 144–148.

11. H. Hiroi, Y. Iwata, S. Adachi, H. Sugimoto, and A. Yamada, "New World-Record Efficiency for Pure-Sulfide Cu(In,Ga)S2 Thin-Film Solar Cell With Cd-Free Buffer Layer via KCN-Free Process," *IEEE Journal of Photovoltaics* 6, no. 3 (2016): 760–763.

12. R. Mallick, X. Li, C. Reich, et al., "Arsenic-Doped CdSeTe Solar Cells Achieve World Record 22.3% Efficiency," *IEEE Journal of Photovoltaics* 13 (2023): 510–515.

13. M. Langenhorst, B. Sautter, R. Schmager, et al., "Energy Yield of All Thin-Film Perovskite/CIGS Tandem Solar Modules," *Progress in Photovoltaics: Research and Applications* 27 (2019): 290–298.

14. J. E. Avon, K. Yoodee, and J. C. Woolley, "Solid Solution, Lattice Parameter Values, and Effects of Electronegativity in the (Cu1−xAgx)(Ga1−yIny)(Se1−zTez)2 Alloys," *Journal of Applied Physics* 55 (1984): 524–535.

15. Z. J. Li-Kao, T. Kobayashi, and T. Nakada, in *Conference Record of the IEEE Photovoltaic Specialists Conference* (2013), 3402.

16. A. M. Gabor, J. R. Tuttle, D. S. Albin, M. A. Contreras, R. Noufi, and A. M. Hermann, "High-Efficiency CuInxGa1−xSe2 Solar Cells Made From (Inx,Ga1−x)2Se3 Precursor Films," *Applied Physics Letters* 65 (1994): 198–200.

17. T. P. Weiss, O. Ramirez, S. Paetel, et al., "Metastable Defects Decrease the Fill Factor of Solar Cells," *Physical Review Applied* 19 (2023): 024052.

18. P. Würfel, "The Chemical Potential of Radiation," *Journal of Physics C: Solid State Physics* 15 (1982): 3967–3985.

19. S. Siebentritt, T. P. Weiss, M. Sood, M. H. Wolter, A. Lomuscio, and O. Ramirez, "How Photoluminescence Can Predict the Efficiency of Solar Cells," *Journal of Physics: Materials* 4 (2021): 042010.

20. M. H. Wolter, B. Bissig, E. Avancini, et al., "Influence of Sodium and Rubidium Postdeposition Treatment on the Quasi-Fermi Level Splitting of Cu(In,Ga)Se2Thin Films," *IEEE Journal of Photovoltaics* 8 (2018): 1320–1325.

21. T. Trupke, R. A. Bardos, M. D. Abbott, and J. E. Cotter, "Suns-Photoluminescence: Contactless Determination of Current-Voltage Characteristics of Silicon Wafers," *Applied Physics Letters* 87 (2005): 093503.

22. F. Babbe, L. Choubrac, and S. Siebentritt, "The Optical Diode Ideality Factor Enables Fast Screening of Semiconductors for Solar Cells," *Solar RRL* 2 (2018): 1800248.

23. U. Rau, B. Blank, T. C. M. Müller, and T. Kirchartz, "Efficiency Potential of Photovoltaic Materials and Devices Unveiled by Detailed-Balance Analysis," *Physical Review Applied* 7 (2017): 044016.

24. C. Hönes, (Diss., University of Luxembourg, 2016).

25. W. E. Vargas, D. E. Azofeifa, and N. Clark, "Retrieved Optical Properties of Thin Films on Absorbing Substrates From Transmittance Measurements by Application of a Spectral Projected Gradient Method," *Thin Solid Films* 425 (2003): 1–8.

26. T. P. Weiss, P. Arnou, M. Melchiorre, et al., "Thin-Film(Sb,Bi)2Se3Semiconducting Layers With Tunable Band Gaps Below 1 eV for Photovoltaic Applications," *Physical Review Applied* 14 (2020): 024014.

27. P. Yu and M. Cardona, *Fundamentals of Semicondcutors*, 4th ed., (Berlin Heidelberg: Springer-Verlag, 2010).

28. D. Regesch, L. Gütay, J. K. Larsen, et al., "Degradation and Passivation of CuInSe2," *Applied Physics Letters* 101 (2012): 112108.

29. F. Babbe, L. Choubrac, and S. Siebentritt, "Quasi Fermi Level Splitting of Cu-Rich and Cu-Poor Cu(In,Ga)Se2 Absorber Layers," *Applied Physics Letters* 109 (2016): 082105.

30. S. Siebentritt, U. Rau, S. Gharabeiki, et al., "Photoluminescence Assessment of Materials for Solar Cell Absorbers," *Faraday Discussions* 239 (2022): 112–129.

31. J. K. Larsen, S. Y. Li, J. J. S. Scragg, et al., "Interference Effects in Photoluminescence Spectra of Cu2ZnSnS4 and Cu(In,Ga)Se2 Thin Films," *Journal of Applied Physics* 118 (2015): 035307.

32. M. H. Wolter, B. Bissig, P. Reinhard, S. Buecheler, P. Jackson, and S. Siebentritt, "Physica Status Solidi (C) Current Topics," *Solid State Physics* 6 (2017): 1600189.

33. U. Rau and J. H. Werner, "Radiative Efficiency Limits of Solar Cells With Lateral Band-Gap Fluctuations," *Applied Physics Letters* 84 (2004): 3735–3737.

34. M. Sood, A. Urbaniak, C. K. Boumenou, et al., "Near Surface Defects: Cause of Deficit Between Internal and External Open-Circuit Voltage in Solar Cells," *Progress in Photovoltaics* 30 (2022): 263–275.

35. R. Scheer and H. W. Schock, *Chalcogenide Photovoltaics: Physics, Technologies, and Thin Film Devices* (Weinheim: Wiley-VCH, 2011).

36. T. Bertram, V. Deprédurand, and S. Siebentritt, in *40th IEEE Photovoltaic Specialist Conference* (IEEE, Denver, 2014), 3633.

37. V. Depredurand, Y. Aida, J. Larsen, A. Majerus, and S. Siebentritt, in *37th IEEE Photovoltaic Specialist Conference* (IEEE, Seattle, 2011), 337.

38. R. T. Ross, "Some Thermodynamics of Photochemical Systems," *The Journal of Chemical Physics* 46 (1967): 4590.

39. M. Maiberg and R. Scheer, "Theoretical Study of Time-Resolved Luminescence in Semiconductors. I. Decay From the Steady State," *Journal of Applied Physics* 116 (2014): 123710.

40. T. Otaredian, "Separate Contactless Measurement of the Bulk Lifetime and the Surface Recombination Velocity by the Harmonic Optical Generation of the Excess Carriers," *Solid State Electronics* 36 (1993): 153–162.

41. T. P. Weiss, B. Bissig, T. Feurer, R. Carron, S. Buecheler, and A. N. Tiwari, "Bulk and Surface Recombination Properties in Thin Film Semiconductors With Different Surface Treatments From Time-Resolved Photoluminescence Measurements," *Scientific Reports* 9 (2019): 5385.

42. M. Maiberg and R. Scheer, "Theoretical Study of Time-Resolved Luminescence in Semiconductors. II. Pulsed Excitation," *Journal of Applied Physics* 116 (2014): 123711.

43. M. Maiberg, T. Hölscher, S. Zahedi-Azad, and R. Scheer, "Theoretical Study of Time-Resolved Luminescence in Semiconductors. III. Trap States in the Band Gap," *Journal of Applied Physics* 118 (2015): 105701.

44. S. J. Heise and J. F. López Salas, "Charge Separation Effects in Time-Resolved Photoluminescence of Cu(In,Ga)Se2 Thin Film Solar Cells," *Thin Solid Films* 633 (2017): 35–39.

45. F. Pianezzi, P. Reinhard, A. Chirilă, et al., "Unveiling the Effects of Post-Deposition Treatment With Different Alkaline Elements on the Electronic Properties of CIGS Thin Film Solar Cells," *Physical Chemistry Chemical Physics* 16 (2014): 8843–8851.

46. T. P. Weiss, F. Ehre, V. Serrano-Escalante, T. Wang, and S. Siebentritt, "Understanding Performance Limitations of Cu(In,Ga)Se2Solar Cells due to Metastable Defects—A Route Toward Higher Efficiencies," *Solar RRL* 5 (2021): 2100063.

47. T. P. Weiss, O. Ramírez, S. Paetel, W. Witten, J. Nishinaga, T. Feurer, and S. Siebentritt, (in revision, 2022).

48. T. Wang, F. Ehre, T. P. Weiss, et al., "Diode Factor in Solar Cells With Metastable Defects and Back Contact Recombination," *Advanced Energy Materials* 12 (2022): 2202076.

49. R. Scheer and H. W. Schock, *Chalcogenide Photovoltaics: Physics, Technologies, and Thin Film Devices* (Weinheim, Germany: Wiley-VCH Verlag & Co. KGaA, 2011).

50. M. Sood, D. Adeleye, S. Shukla, T. Törndahl, A. Hultqvist, and S. Siebentritt, "Faraday Discussions," (2022).

51. J. Keller, K. V. Sopiha, O. Stolt, et al., "Wide-gap (Ag,Cu)(In,Ga)Se2 Solar Cells With Different Buffer Materials—A Path to a Better Heterojunction," *Progress in Photovoltaics: Research and Applications* 28 (2020): 237–250.

52. M. Sood, P. Gnanasambandan, D. Adeleye, et al., "Electrical Barriers and Their Elimination by Tuning (Zn,Mg)O Buffer Composition in Cu(In,Ga)S2 Solar Cells: Systematic Approach to Achieve Over 14% Power Conversion Efficiency," *Journal of Physics: Energy* 4 (2022): 045005.

53. T. Kirchartz and U. Rau, "What Makes a Good Solar Cell?" *Advanced Energy Materials* 8 (2018): 1703385.

Supporting Information

Additional supporting information can be found online in the Supporting Information section.

Appendix A

A Tandem Efficiency Calculation

The calculation of the tandem efficiencies shown in Figure 1 are based on the approach described in Ref. [53] for a single-junction solar cell. In particular, the metrics of the current–voltage characteristics are calculated using the following expressions [53]:

$$\Phi_{BB} = \frac{2\pi E^2}{h^3 c^2} \frac{1}{\exp\frac{E}{k_B T} - 1} \tag{A1}$$

$$J_{0,SQ} = q \int_{E_g}^{E_{UL}} dE \Phi_{BB}(E) \tag{A2}$$

$$J_{SC,SQ} = \int_{E_g}^{E_{UL}} dE \Phi_{sun}(E) \tag{A3}$$

The upper limit (UL) for the integration is set to E_{UL}. For a single-junction solar cell or a top-cell in a tandem configuration, E_{UL} is set to ∞. For a bottom-cell, $E_{UL} = E_{g,top}$, which reflects the fact that no photons from Φ_{sun} enter the bottom cell after perfect absorption by the top cell.

$$V_{OC,SQ} = k_B T \ln\left(\frac{J_{SC,SQ}}{J_{0,SQ}} + 1\right) \tag{A4}$$

The fill factor is determined from the maximum power point (MPP) as.

$$FF = \frac{P_{MPP}}{J_{SC,SQ} V_{OC,SQ}} \tag{A5}$$

using the following current–voltage characteristics

$$J(V) = J_{0,SQ}\left(\exp\left(\frac{V}{k_B T}\right) - 1\right) - J_{SC,SQ} \tag{A6}$$

Finally, the efficiencies for the 2T and 4T configuration are calculated. In the case of the 4T device, the efficiencies for the top- and bottom-cell are added, where the individual efficiencies η are obtained via

$$\eta = \frac{V_{OC,SQ} J_{SC,SQ} FF}{P_{sun}} \tag{A7}$$

In the case of the 2T device, $J_{SC,SQ,2T}$ and $J_{0,SQ,2T}$ need to be determined first, which is done according to

$$J_{SC,SQ,2T} = \min\left(J_{SC,top}, J_{SC,bottom}\right) \tag{A8}$$

$$J_{0,SQ,2T} = \frac{J_{0,top} J_{0,bottom}}{J_{SC,SQ,2T}} \tag{A9}$$

Expression (A8) enforces *current-matching*, i.e., the overall current density is limited by the smaller current density due to the series connection of the cells. Expression (A9) results in a $V_{OC,2T}$ determined by the addition of the V_{OC}'s of the individual sub-cells. Subsequently, the FF, $J(V)$ and the efficiency is calculated by Equations (A5) and (A6) as described above.